

Review

First Experiments in Structural Biology at the European X-ray Free-Electron Laser

Grant Mills ^{1,*}, Richard Bean ¹ and Adrian P. Mancuso ^{1,2}

¹ European X-Ray Free-Electron Laser Facility GmbH, Holzkoppel 4, 22869 Schenefeld, Germany; richard.bean@xfel.eu (R.B.); adrian.mancuso@xfel.eu (A.P.M.)

² Department of Chemistry and Physics, La Trobe Institute for Molecular Science, La Trobe University, Melbourne, VIC 3086, Australia

* Correspondence: grant.mills@xfel.eu

Received: 24 April 2020; Accepted: 18 May 2020; Published: 25 May 2020



Abstract: Ultrabright pulses produced in X-ray free-electron lasers (XFELs) offer new possibilities for industry and research, particularly for biochemistry and pharmaceuticals. The unprecedented brilliance of these next-generation sources enables structure determination from sub-micron crystals as well as radiation-sensitive proteins. The European X-Ray Free-Electron Laser (EuXFEL), with its first light in 2017, ushered in a new era for ultrabright X-ray sources by providing an unparalleled megahertz-pulse repetition rate, with orders of magnitude more pulses per second than previous XFEL sources. This rapid pulse frequency has significant implications for structure determination; not only will data collection be faster (resulting in more structures per unit time), but experiments requiring large quantities of data, such as time-resolved structures, become feasible in a reasonable amount of experimental time. Early experiments at the SPB/SFX instrument of the EuXFEL demonstrate how such closely-spaced pulses can be successfully implemented in otherwise challenging experiments, such as time-resolved studies.

Keywords: X-ray free-electron laser; European XFEL; serial crystallography; time-resolved structural biology

1. Structural Biology at XFEL Sources

1.1. X-ray Sources and Crystallography

X-ray based methods have a rich history of contributing to biological structure determination. The first structural images of DNA, for example, were published in 1953, guided by X-ray crystallographic data [1,2], a success that still captures the public's imagination.

In more recent decades, large-scale, multi-user synchrotron facilities have been the driving technology behind X-ray structural biology investigation and have become the cornerstone for protein research [3]. Since experiment stations dedicated to macromolecular crystallography (MX) first appeared at synchrotron facilities in the 1970s, these facilities have been the go-to tool for crystallographers [4,5]. Synchrotrons offered a fundamental improvement in the X-ray photon flux and enabled routine atomic structure determination of biological macromolecules as well as new, tunable wavelength-based experimental phasing methods, such as single- and multi-wavelength anomalous dispersion (SAD and MAD) [6–8]. Modern third-generation synchrotrons—such as the European Synchrotron Radiation Facility (ESRF) in France [9], the Advanced Photon Source (APS) at Argonne National Laboratory in the USA [10], the Super Photon Ring-8 GeV (SPring-8) in Japan [11], and PETRA III at Deutsches Elektronen-Synchrotron (DESY) in Germany [12]—can produce an average brilliance of up to 10^{19} – 10^{20} photons s^{-1} $mrad^{-2}$ mm^{-2} 0.1% bandwidth⁻¹ [13] offering ample photons for traditional structure determination using relatively large crystals of macromolecules.

X-ray free electron lasers (XFELs) are the next generation of brighter X-ray sources. With up to a 10^9 increase in brilliance over synchrotron sources, XFELs enable the development of new methods to study ultrafast processes, structural changes, and biological reactions at biologically relevant timescales [14–16], all from crystals that can be much smaller than those traditionally used at synchrotron sources.

1.2. Free Electron Lasers (FELs)

XFELs produce ultrashort pulses, often only ~50 fs long, or in some cases even shorter. These pulses are produced by the self-amplified spontaneous emission (SASE) process [17]. The duration of these pulses is so short that, for many physical processes, the pulse itself acts like a fast camera shutter. The pulse duration captures a single *snapshot* of the target sample. Any finite pulse duration that is not time-resolved on detection will time-average the data over its total pulse length; however, since molecular motion typically occurs within hundreds of femtoseconds or longer [18], the ~50 fs pulse length can be considered a practically static image in many cases. Producing these very short pulses is technically possible at synchrotrons—but only by sacrificing the comparatively lower peak intensity by a further three orders of magnitude [13,19].

1.3. Structural Biology Experiments at XFEL Sources

Traditional synchrotron-based crystallography experiments often use individual crystals mounted on goniometers to sample the rocking curve in order to measure a complete set of diffraction spot intensities [20]. Rotation of the crystal during each detector integration window (i.e. exposure) allows for measurement of the full scattering intensity of each Bragg reflection. Typically, a dataset comprises a few hundred detector images, each with an integration window of hundreds of milliseconds to seconds.

Due to the high brilliance and X-ray pulse delivery patterns, macromolecular crystallography experiments at FEL sources typically employ a serial approach where each recorded diffraction image is produced from a new crystal, a method known as serial femtosecond crystallography (SFX) [21,22]. Diffraction from each FEL pulse is recorded into a separate detector image, where the short pulse lengths ‘snap-shot’ a crystal in a random orientation, recording only partial interactions of reciprocal lattice points and the Ewald sphere. Often, detector frames in excess of 10,000 are integrated to form a single complete dataset to account for the stochastic nature of the data collection [23]. FEL sources have the high intensity and short pulse durations necessary for high-resolution, time-resolved studies.

Serial crystallography type experiments have also been successfully performed at synchrotron sources, often requiring concessions to beam intensity and/or bandwidth [24,25].

The significantly large increase in peak brilliance of XFELs potentially provides crystallographers with an opportunity to complete otherwise impossible projects. Diffraction data from small nanocrystals typically require a brilliance not available at synchrotron sources. XFELs provide a feasible way to measure diffraction from crystals as small as 5 μm [22] and in some cases even nanocrystals [26].

A number of variables contribute to the ultimate resolution of a crystallographic dataset, and there is a broad body of work that considers the intrinsic nature of crystal diffraction [27–30]. Though beyond the scope of this review, broadly speaking, smaller crystals often yield poorer results than larger crystals from the same type of molecule. As the number of unit cells within the crystal increases by N , the signal recorded is amplified by approximately N^2 . Producing protein crystals large enough for use in common crystallographic experiments can be a major hurdle for many projects. Significant time, cost, and optimization are needed to produce purified recombinant protein and, even with purified protein, unfortunately, crystallization processes do not always produce usable, diffracting crystals [31–33].

Serial femtosecond crystallography is a variant of crystallography that, as the name suggests, uses a serial approach to data collection in which crystals are injected into interaction region, typically via a liquid medium, and are then exposed to incident X-ray pulses resulting in a single crystal

diffraction event [21,34]. Notably, the liquid medium and surrounding gas used also scatters photons and causes an increase in the detected background signal. SFX injection techniques often optimize jet size to crystal size in order to minimize the background scatter and make post-experiment analysis easier. Best injection practices aim to maximize the stable jet length and delay the Rayleigh breakup point, where droplet formations occur, Figure 1 [35–39]. Droplets formed have a diameter about 40% larger than the jet diameter and therefore contribute to more background signal. Furthermore, they are only present when the beam arrives some of the time, so without explicit timing, the proportion of pulses that intersect liquid containing crystal decreases. Additionally, the energy deposited into the liquid jet by an FEL X-ray pulse causes jet instability via rapid and violent vaporization, destroying the local stable region and the sample. Any liquid-jetting technology needs to account for these difficulties [38].

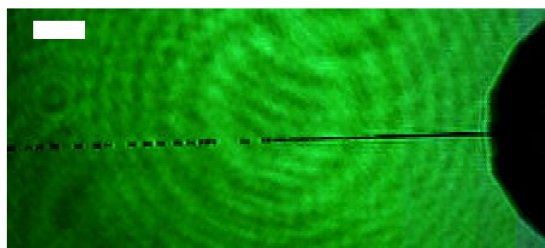


Figure 1. The Rayleigh breakup point can be seen where the stable liquid jet forms discrete droplets. The Rayleigh breakup length, or jet length, for a given solution is related to the jet diameter and the jet speed. Scale bar: 100 μm . Figure originally published in Opt. Express [35].

A jet's speed is a typical variable that is (indirectly) controlled to influence jet stability and hence suitability for a given experiment. Early predictions suggest that, for a liquid jet to be stable and provide an experimentally fresh sample into the interaction region at a ~ 1 MHz repetition rate, it would have to travel a minimum of 100 μm [40] between subsequent pulses and commensurately faster to leverage the full 4.5 MHz repetition rate of the EuXFEL [41]. The speeds necessary for this to occur at lower-repetition-rate FELs, such as the Linac Coherent Light Source (LCLS) at the SLAC National Accelerator Laboratory in the USA, is only 0.012 m s^{-1} [41]. As predicted, success at LCLS was achieved with jet speeds of 10 m s^{-1} [21], a speed so much higher than the minimum required value that the FEL pulse rate can be considered insignificant to the jet speed and stability. Prior to first experiments at EuXFEL, the typical jet speeds used at other XFELs, about 10 m s^{-1} or slower, raised an obvious and valid question about sample delivery at EuXFEL: Is it possible to produce functional and stable jets fast enough to utilize the MHz pulse structure and therefore capitalize on the vastly improved data collection rate?

1.4. The European XFEL (EuXFEL)

The EuXFEL is the world's first MHz-pulse-rate hard XFEL, consisting of a 1700 m supercooled linear accelerator (LINAC) and generating up to 17.5 GeV electron bunches. The electron bunches emit photons when passed through an undulator, which is finely tuned to control the photon emission [17,42]. The EuXFEL currently operates three undulators to serve six different instruments. The focus of this review is limited to one—the Single Particles, Clusters, and Biomolecules/Serial Femtosecond Crystallography (SPB/SFX) instrument, Figure 2—which addresses the field of XFEL structural biology. The SPB/SFX instrument is downstream from the so-called SASE1 undulator, which can produce photons of tunable energies in a range broader than the SPB/SFX instrument's operating range of 5–16 keV (and perhaps down to 3 keV with further commissioning and certain limitations). The machine is designed to produce X-ray pulses at a peak brilliance of 5×10^{33} photons s^{-1} mrad^{-2} mm^{-2} 0.1% bandwidth $^{-1}$ [13,43,44], approximately nine orders of magnitude brighter than that of current-generation synchrotron sources. Observations at the SASE1

undulator have shown 4 mJ pulses at 6 keV photon energy, which correspond to about 4×10^{12} photons per pulse. If we assume a pulse duration of 30 fs, we find that for an approximately 3 mm diameter beam near the instrument (about 900 m from the source), the brilliance is about 2.25×10^{33} photons s^{-1} mm^{-2} $mrad^{-2}$ 0.1% bandwidth $^{-1}$. This peak brilliance is comparable with other XFEL sources, particularly LCLS [45], but the unique MHz repetition rate at the EuXFEL is currently not available at any other facility.

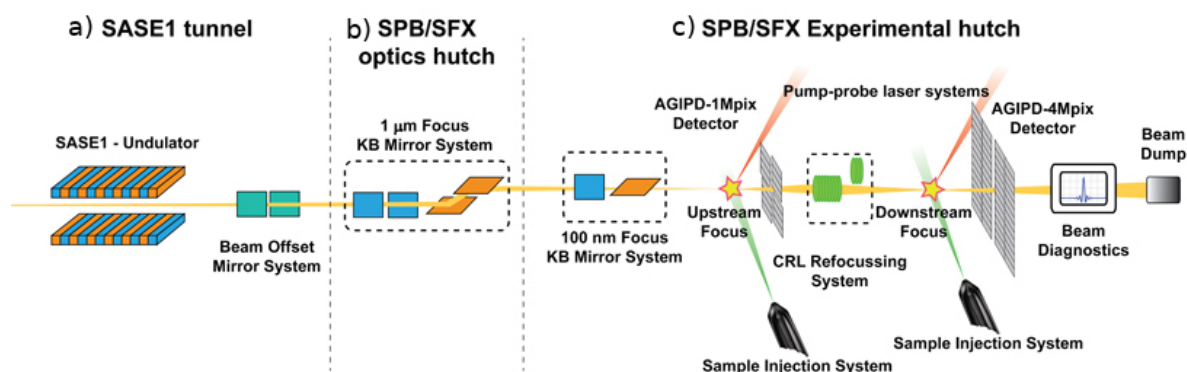


Figure 2. The Single Particles, Clusters, and Biomolecules and Serial Femtosecond Crystallography (SPB/SFX) instrument is divided into three main components: (a) The tunnel containing the SASE1 (self-amplified spontaneous emission) undulator and offset mirrors. The offset mirrors remove very hard X-ray higher harmonic radiation and guide the wanted X-rays onto downstream focusing optics. (b) The X-ray beam then enters the optics hutch, which contains the 1 μ m-scale KB focusing mirror system. (c) The experiment hutch contains the 100 nm-scale KB focusing mirror system, the upstream interaction region where samples interact with the X-ray beam, AGIPD-1M detector, compound refractive lens (CRL) refocusing system, AGIPD-4M detector, and downstream beam diagnostics.

MHz-repetition-rate hard X-ray sources provide unprecedented data collection rates and enable investigation of difficult and previously infeasible projects, such as time-resolved studies, so-called mixing experiments (where a protein crystal is mixed with a potential ligand, for example), or simply small crystal samples, within an experimentally feasible time frame [13,44]. The MHz repetition rate can also be coupled with an optical laser pump–X-ray probe scheme with femtosecond time-delay resolution, as shown by Sato et al. [46] Static samples, or samples which are not continuously refreshed, that do not recover to the ground state between MHz-rate pulses can also be studied by modifying the pulse pattern to account for the longer recovery period at the cost of the data collection rate.

A novel, 1 Mpx Adaptive Gain Integrating Pixel Detector (AGIPD-1M) [47] has been developed to record individual scattering events. AGIPD-1M is capable of recording 4.5 MHz in three gain stages [48]. As each pixel is capable of selecting a gain stage appropriate for its level of signal—independently of surrounding pixels—low-intensity signals at higher resolution can be recorded, while simultaneously recording the low-resolution, high-intensity reflections.

1.5. Diffraction Before Destruction

XFELs with a lower pulse repetition rate (≤ 120 Hz) are able to renew the sample interaction region prior to subsequent pulses and are capable of maintaining a stable sample supply with the use of liquid injector solutions, such as Gas Dynamic Virtual Nozzles (GDVNs) [49]. However, until first operation of the EuXFEL, sample refresh rates have never been tested at MHz repetition, and it is not certain that previously successful techniques, such as those performed at LCLS, would maintain the same consistency in data collection.

While offline testing (and indeed initial experiments) has demonstrated that liquid jets can be made fast enough to replenish the sample (Figure 3), it is not sufficient to simply refresh the space with a fresh sample. The microcrystals within the liquid medium also need to remain intact. Prior to the

first MHz repetition rate experiments at the EuXFEL, it was unknown whether crystal samples could withstand the possible acoustic shock that propagates back along the liquid jet due to the explosion of the sample. Indeed, there is evidence to suggest that it may be possible for the shock wave to travel upstream along the liquid jet and disrupt the crystals in the fresh sample entering the interaction region, Figure 4 [40]. The energy deposited into the jet by the XFEL beam depends on a number of parameters. The most obvious is the pulse energy of the illuminating X-ray beam in conjunction with the focal size if the focal size is larger than the jet width. Perhaps the most critical parameter is the diameter of the liquid jet at the point of interaction with the X-ray beam. In a publication by Stan et al. [40], the liquid jet diameters were between 3 and 20 μm with a fastest jet speed of 33.6 m s^{-1} . For a liquid jet to be compatible with even 1.1 MHz repetition rates, the jet speed would need to be at least 50 m s^{-1} —about twice as fast than described in [40]. Faster jets tend to be narrower and, in a fortunate direction of scaling, the energy into the liquid jet scales with the n th power of the liquid jet diameter [40]. Prior to first experiments at EuXFEL, it was not known if this weaker shock wave causes any measurable effect on the diffraction quality of sample crystals.

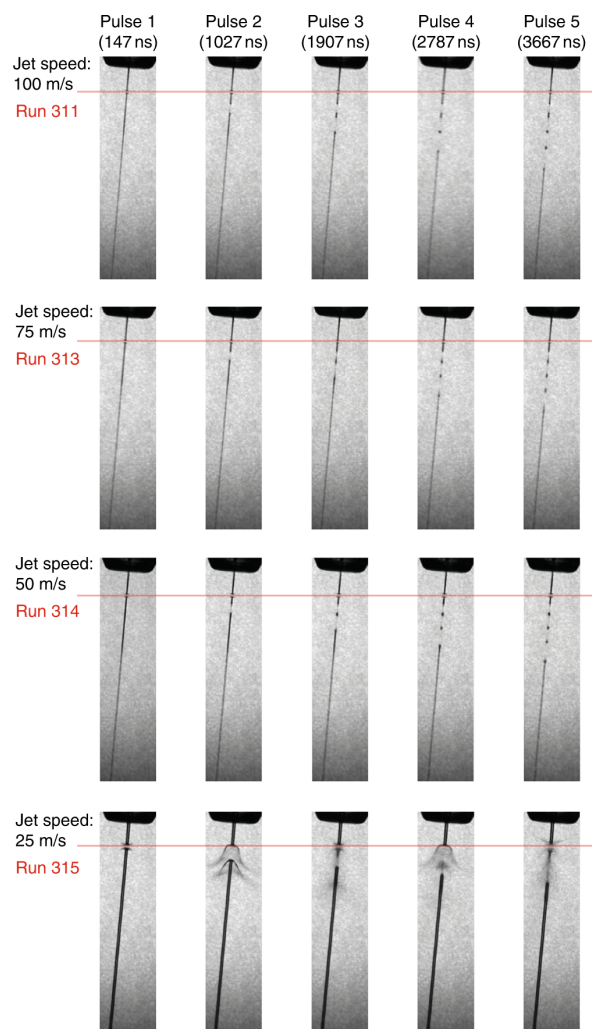


Figure 3. Pulsed illumination of the sample interaction region shows how X-ray pulses vaporize the sample, creating voids. Jet speeds of 100, 75, and 50 m s^{-1} refresh the interaction region before the arrival of the subsequent pulse. It can be seen that the lower limit for 1.1 MHz operation falls between 25 and 50 m s^{-1} . Figure originally published in Nat. Commun. [50].

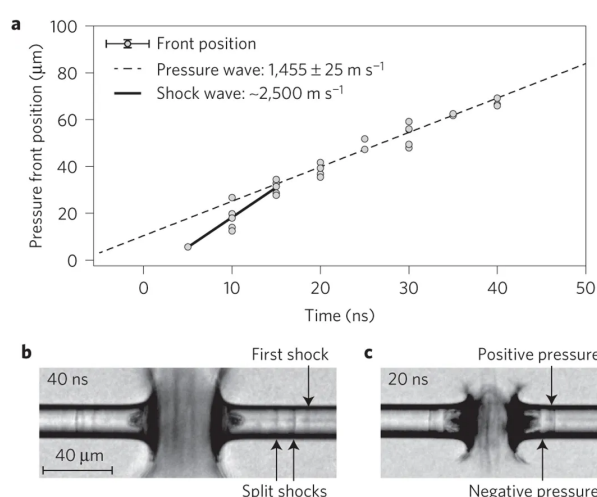


Figure 4. Graph (a) plots the position of the first pressure front seen in (b) as a function of time. Images (b,c) show still frames of an otherwise stable liquid jet, exploding from the X-ray pulse. Shock waves split into multiple pressure fronts and travel transversely along the liquid jet. Figure originally published in Nat. Phys. [40].

1.6. First User Experiments at the EuXFEL

The EuXFEL produced its first light in May 2017. The following September, first user experiments were performed at the SPB/SFX instrument [44,50,51]. Perhaps unsurprisingly, one of the first research questions asked was whether MHz repetition rate pulse trains can be usefully employed for structural biology using serial crystallography with liquid jet sample delivery. The very first experiment undertaken at SPB/SFX (published by Wiedorn et al. [50]) and a later, similar experiment (published by Gruenbein et al. [51]) used a 1.1 MHz pulse train consisting of 30 and 50 pulses, respectively, to record crystallographic diffraction data of lysozyme. During these first experiments, the smallest focus achievable on the temporary CRL optics was 15 μm.

Analysis of the scattering produced from each pulse in the pulse train supported a successful proof of concept. The faster jetting speeds were capable of maintaining a stable sample interaction region with no measurable change in the data quality between first and subsequent pulses in a pulse train. Figure 5, reproduced from [50], shows a metric based on diffraction statistics as a function of pulse number that is essentially constant over the train. Figure 6, reproduced from [51], shows a histogram of resolutions for all first and second pulses, again emphasizing the equivalence of first and second (and hence subsequent) pulses in the train for structure determination. Hence, for the conditions used in these experiments, one concludes it is possible to use the entire pulse train for structure determination, and hence to leverage the many more pulses per unit time delivered by the EuXFEL.

Furthermore, Gruenbein et al. also described a lack of radiation damage as measured from the disulphide bonds lengths found in hen egg-white lysozyme (HEWL); such lengths remained within acceptable ranges, Figure 6.

Wiedorn et al. collected 3,215,616 diffraction images from an additional sample: CTX-M-14 β-lactamase crystals. The crystals were approximately 3–8 μm in size, of which 12,474 images contained useful data resulting in a 1.7 Å structure. Gruenbein et al. collected a total of 1,333,750 images for Concanavalin A and B, of which 76,803 and 23,719 contained indexable data, resulting in 2.2 Å and 2.1 Å structures, respectively. Gruenbein et al. further described how a measurable decrease of intensity across the pulse train impacts statistical analysis. Their experiment consisted of a first-pulse average intensity around 1.6 mJ, which dropped approximately logarithmically to 1.4 mJ by the end of the pulse train. They concluded that the fluctuations in hit rate, signal to noise, R split, and B-factors over this energy range were not significant enough to hinder the resolution of their electron density maps.

Both Wiedorn et al. and Gruenbein et al. were able to utilize the entire pulse train of 1.1 MHz [50,51]. Wiedorn et al. performed a systematic study of how gas dynamic virtual nozzle (GDVN) jet speed affects data collection, Figure 3. Interactions between the sample jet and the first five X-ray pulses within each train were recorded using a pulsed illumination laser. The illumination laser was able to record voids formed in the jet by the superheating of the X-ray pulse. As the time between pulses remained constant, Wiedorn et al. were able to record the jet speed by measuring the distance between subsequent voids in the jet. Correlating the jet speeds of 100, 75, 50, and 25 m s^{-1} and the likelihood of a recorded diffraction pattern of a specific pulse number revealed that jets between 50 and 100 m s^{-1} were able to recover in time for the subsequent X-ray pulse; notably, these speeds were significantly slower than predictions by Chavas et al. [41]. While these predictions were useful in defining the range of possible speeds, it is likely that the assumption of the 100 μm distance between jet explosions was overestimated. These were the first experiments validating the capabilities of MHz repetition rate serial femtosecond crystallography.

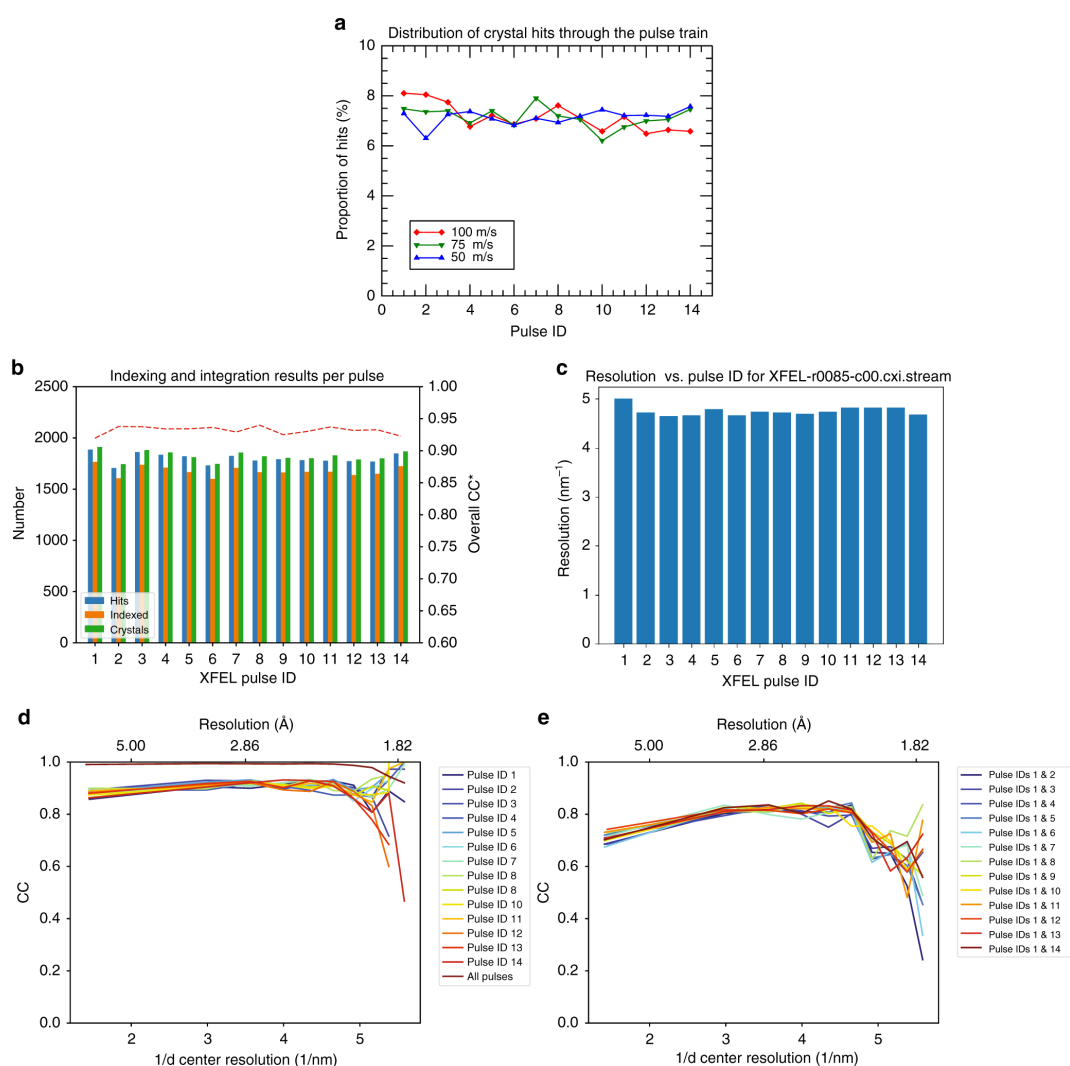


Figure 5. Graph (a) and histograms (b,c) suggest a stable sample delivery system with an approximately equal probability of a diffraction event across the pulse train. Graphs (d,e) show data quality metrics as a function of resolution. Figure originally published in Nat. Commun. [50].

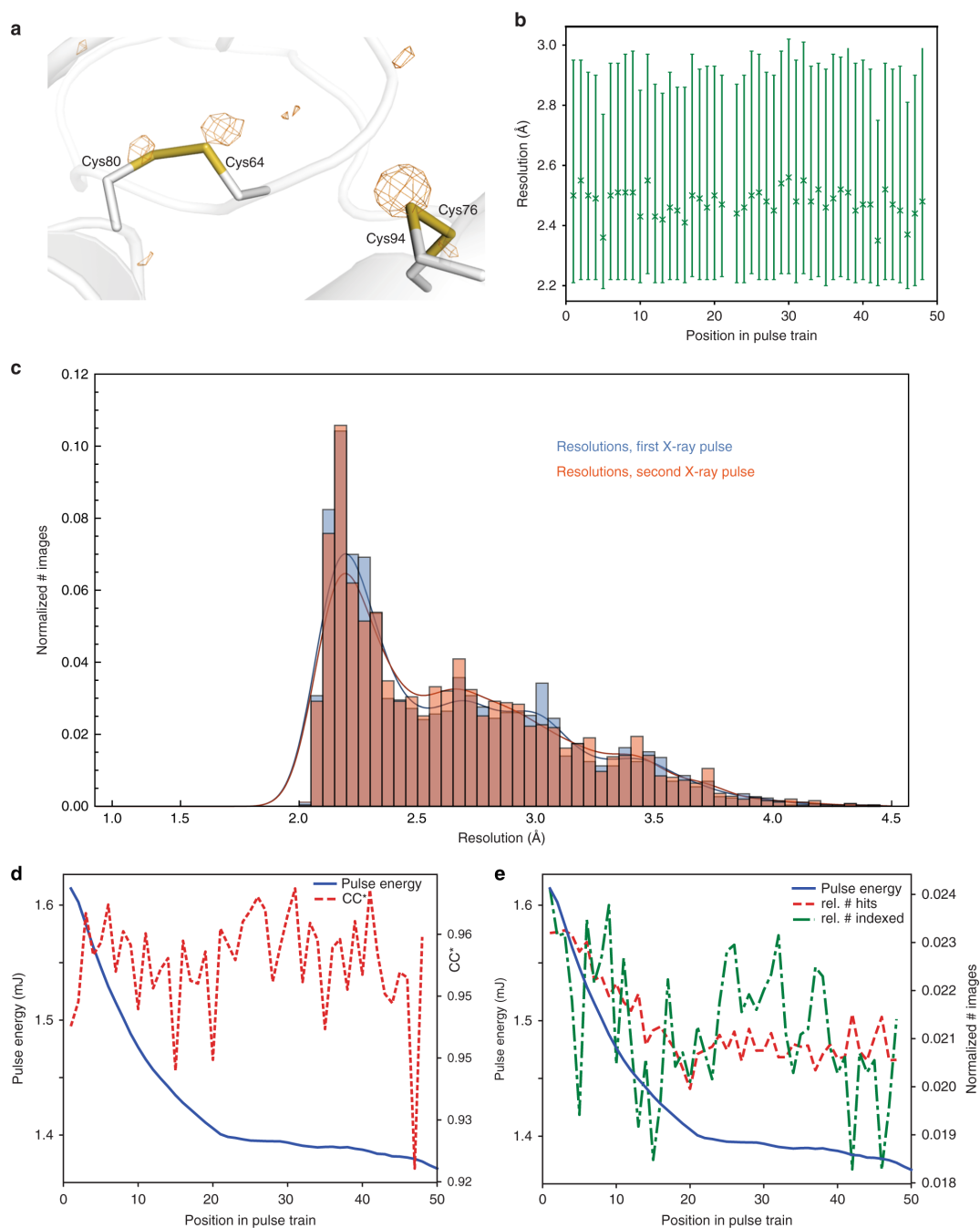


Figure 6. Image (a) and graph (b) show the length measurements of disulphide bonds per pulse. Both length and standard deviation are similar across all pulses. Histogram (c) highlights the similarities in data between the first and second pulse; these similarities can be extended to subsequent pulses, as shown in (d,e). Figure originally published in Nat. Commun. [51].

1.7. Pulse-by-Pulse Analysis within the Pulse Train

The first experiments were a proof of concept of the sample injection speeds, data collection, and rapid detector operation for the first 50 pulses. Nevertheless, they had two major limitations that limit the general conclusions that can be drawn. The pulse energy and focal spot sizes used in the experiments were non-optimal. The average pulse energies were not particularly high in either cases, 580 and 1400 μJ , and the focus was perhaps a factor of 25 larger than nominal. This limits the strength of any conclusion regarding potential damage from a shock wave induced by the incident XFEL pulse. Secondly, while various metrics demonstrate that the differences in data between first

and subsequent pulses are negligible, not enough data were collected in either experiment to produce individual structures from each set of first pulses, second pulses, and so forth.

Yefanov et al. extended the early success of these first two published experiments by collecting sufficient data to determine a structure from each of 120 pulses in a pulse train [52]. Yefanov et al. collected 16 million data frames of HEWL crystals using 120 pulses at a 1.1 MHz pulse rate. From the 16 million total data frames collected, they were able to attribute approximately 7000 indexable hits across each of the pulses within the train. Analyzing the data by pulse number allowed pulse-dependent structural analysis and a deeper insight into data quality. Yefanov et al. were able to create a protein structure from each pulse number in the train, a notable step further than the results documented in the Wiedorn and Gruenbein publications, and ultimately concluded that the data quality was consistent across the entire train, Figure 7.

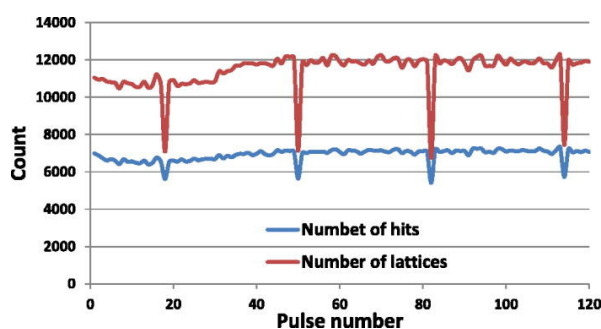


Figure 7. Number of hits and indexed lattices plotted against pulse number. The decreases in hits at pulses 18, 50, 82, and 114 can be attributed to a systematic artifact in detector operation, which was subsequently corrected. The likelihood of any one pulse hitting a crystal is stochastic in nature, as shown by the relatively even distribution across the pulse train. Figure originally published in *Struct. Dyn.* [52]; licensed under a Creative Commons Attribution (CC BY) license.

High-resolution data were geometrically limited to 1.7 Å by both the solid angle subtended by the detector and the maximum angle of diffraction unobscured by the exit cone of the sample injection catcher; a device used to minimize contamination of the sample chamber area. Yefanov et al. noted that optimization of the sample injection catcher position and/or changing to shorter X-ray wavelengths would result in higher measured resolution [52]. The assumption of a possible increase of resolution is supported by statistical evidence, R_{split} and CC^* of 1.8 and 0.9999, respectively, across all resolution shells and pulse numbers, Figure 8. A structure from each pulse was determined via molecular replacement and illustrated the independence of each pulse as they “show no meaningful degradation in data quality within the pulse train” and no significant difference in structural distances and angles [52].

Yefanov et al. also showed how a single 30-minute data collection period can result in over 2 million detector images, yielding 190,000 diffraction patterns. Fast data collection, such as this, provides an example for how MHz SFX can be used to collect vast amounts of data, large enough to determine the small changes in structure factors necessary to interpret time-resolved experimental data within feasible periods of experimental time. They explain how the signal-to-noise ratio is vastly improved with an increased amount of data; for example, a 10-minute data run containing 117,415 indexable images resulted in a signal-to-noise ratio of 15 across the detector, which then increased to 48 when considering all collected data (1,374,785 images). Yefanov et al. concluded that the experimental setup used at the EuXFEL showed no significant differences in data quality or in the resolved structures up to the geometry-limited 1.7 Å, and it was therefore also possible to measure time-resolved structures from each pulse. The increase in data volume showed a significant improvement in overall data quality as compared to previously available lower-repetition-rate XFEL experiments. Indeed, it is not surprising that more data provided better statistical analysis. Yefanov et al. showed that, for a given amount of experimental time, it was possible for the EuXFEL to

enable data collection at a rate 30 times faster than other available XFEL sources, paving the way for time-resolved structure determination within a reasonable experimental time period. The significant increase in useful data collection rates from smaller crystals means normally difficult, yet desirable, experiments such as membrane protein structural determination are more likely to be feasible. Currently, most membrane protein crystals are delivered within high viscosity media, such as Lipid Cubic Phase (LCP) [53,54] which restricts how fast they can be injected. Non-viscous media-carrying membrane crystals have shown great success at FELs [21,55], and the advent of high velocity viscous sample delivery will advance the structural determination of membrane protein significantly.

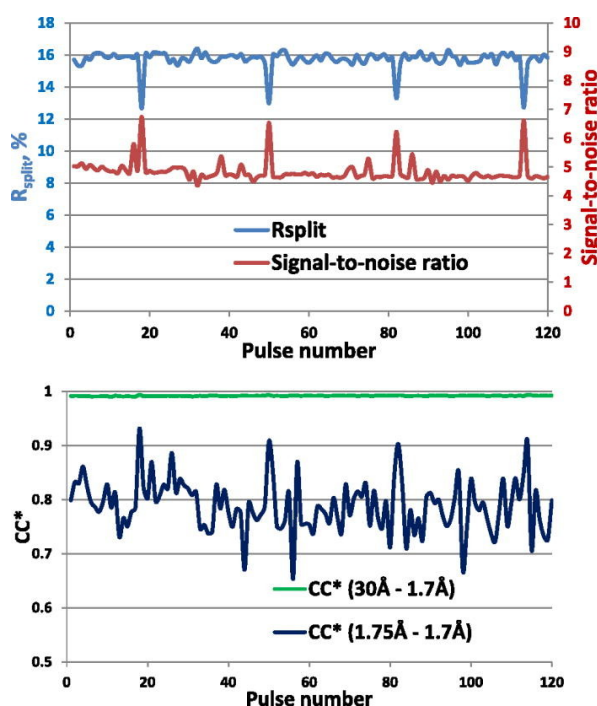


Figure 8. Data quality metrics, as determined from each pulse number, show that the structural data are independent of pulse number and that there is no systematic change in data quality across the train. Any section of the train can be utilized for data collection without compromise. Notably, the repetitive dips in data quality were due to known detector behavior and not due to the experiment itself. Figure originally published in Struct. Dyn. [52]; licensed under a Creative Commons Attribution (CC BY) license.

1.8. Membrane Protein Serial Crystallography at MHz Rates

Since membrane proteins generally have low expression levels, it is difficult to yield a large amount of protein for crystallization. Furthermore, crystallization often results in small crystals with large cell dimensions, and hence very few unit cells within a given crystal. For most traditional X-ray sources, a best-case scenario may still result in low-resolution data, as diffraction intensity is related, approximately, to the square of the number of unit cells. For example, photosystem I (PSI, or plastocyanin-ferredoxin oxidoreductase) belongs to a monoclinic crystal system with unit cell parameters of $a = 279$, $b = 165$, $c = 284$ Å and $\beta = 119.3^\circ$ [56], and lysozyme belonging to a tetragonal crystal system with unit cell parameters of $a = b = 79.2$ and $c = 37.7$ Å [57]. One would expect the lysozyme to provide stronger reflections, as the unit cell is approximately 46 times smaller in volume than the PSI. The N^2 rule of thumb would suggest the measured data to be 46^2 , or approximately 2136 times weaker from the larger unit cell. [58].

Experiments by Gisriel et al. successfully recorded diffraction images of crystallized cyanobacterial PSI at the EuXFEL using $5 \times 5 \times 15 \mu\text{m}^3$ crystals [56]. The collected data were comparable with previously studied synchrotron data measuring a cell dimension of 279, 165, 284 Å, suggesting similar

crystallization and cell packing. Supplementary data provided by Gisriel et al. stated that this was approximately 33 unit cells per crystal, while the lysozyme data studied by Wiedorn et al. were approximately 1400 unit cells. However, despite the significant decrease in the number of unit cells, Gisriel et al. were able to determine the molecular structure to 2.9 Å resolution. Data were collected with 30 pulses per train at 1.1 MHz using a sample injection speed of 50 m s⁻¹. They collected 7,719,186 images of PSI over a selection of detector distances to the sample (168, 233, and 327 mm). The 168 mm dataset was shown to contain significant overlap of Bragg reflections in the low-resolution shells. So-called *spot overlap* creates difficulties in determining the local background and peak intensity. Extreme cases can result in multiple indistinguishable peaks measured as a single spot. Pixel size and unit cell size dictate how close a detector can be moved for a given sample and are therefore a limiting factor in maximum resolution of the data. As the detector distance is decreased, the solid angle across a given pixel as seen from the interaction region becomes greater, meaning any reflections measured within that solid angle will be integrated by a single pixel. Conversely, the solid angle is decreased as the detector-to-sample distance is increased, providing better peak separation as measured by the number of pixels. However, moving the detector further away from the sample also limits the total solid angle of the entire detector and therefore decreases the highest possible resolution. In conjunction with crystal quality and injection methods, consideration of detector position and pixel size is crucial to record the highest quality data possible.

The successful indexing of the 233 and 327 mm sample-to-detector distance datasets was then compared to synchrotron data collected at ESRF [59]. By restricting the data to equal resolution, it was found that the EuXFEL data were similar and representative of the previous studies. Not surprisingly, some differences were measured in the Wilson B-factors. The change in B-factors is related to the different environmental temperatures of the experiment. SFX experiments are typically carried out at room temperature, while most synchrotron MX experiments are cryo-cooled. Room-temperature experiments are often preferred, as they are much closer to biologically relevant temperatures and therefore hypothesized to be much better for structure–function analysis. SFX experiments, as exemplified herein, may provide information that is more biologically relevant than equivalent cryo-temperature experiments if all else is equal. Changes in the temperature of the crystal, and therefore the molecular motion, can be seen in the measured B-factors [60,61]. In other words, as temperature increases, so does the isotropic atomic motion. If a sample is measured at its biologically relevant temperature, the data may also provide more accurate information of protein dynamics.

Further comparing the EuXFEL data to the ESRF data reveals that Gisriel et al. were also able to collect significantly more data, as shown by the multiplicity values of 213 and 3.6, respectively. The stochastic nature of SFX data collection, in general, often results in excess data; however, as the sample is not exposed repetitively and therefore does not suffer radiation damage in the process, these excess data continue to improve data quality. The improvements in XFEL data quality when compared to similar synchrotron data are exemplified by Gisriel et al. and echoed in Table 1 [56].

Table 1. Comparing typical data collection strategies of an X-ray free electron laser (XFEL) source and a synchrotron source shows how repeated measurements improve statistics in the former. A dataset collected at the European XFEL (EuXFEL) by Gisriel et al. measured approximately 60 times more reflections than a typical synchrotron data collection strategy, as shown by the multiplicity values, while also improving on the data quality indicators. Table adapted from Nat. Commun. [56].

	XFEL	Synchrotron
Completeness(%)	100 (100)	99.6 (98.3)
Multiplicity	213 (122)	3.6 (1.9)
CC _{1/2}	0.88 (0.051)	0.633 (0.655)
CC*	0.97 (0.31)	0.991 (0.890)

Figure 9 exemplifies a small section of a single image recorded by AGIPD-1M. The image highlights how AGIPD-1M is capable of recording across multiple gain stages with an effective dynamic range of up to 10^4 photons per pixel. This allows the detection, in a single frame, of even very small signals in some pixels while not saturating the lower resolution shells in other pixels.

Bringing all these components together resulted in the first membrane structure determination by MHz repetition rate serial crystallography, with the room-temperature structure of PSI determined to 2.9 Å resolution [56].

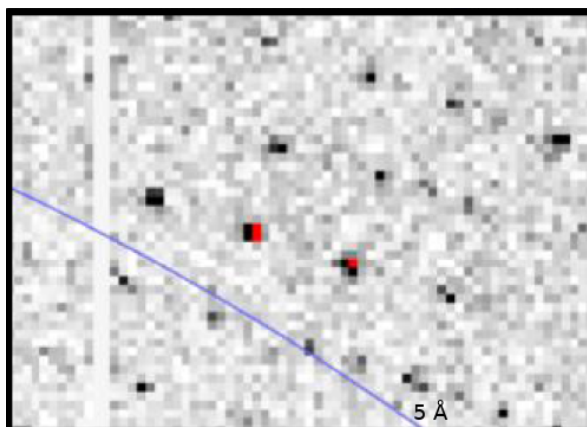


Figure 9. Zoomed lysozyme diffraction pattern recorded on the AGIPD-1M detector. Gray-scale pixel intensity is measured in the “high” gain stage. Pixels colored red have been measured in the “medium” gain stage. Figure modified from original publication in Nat. Commun. [56].

1.9. Time-Resolved Serial Crystallography at MHz Rates

We have seen from the previous examples that the SPB/SFX instrument at the EuXFEL enables a much faster throughput approach to XFEL structural biology than previously available. This vastly improved data collection rate is of extreme benefit for investigating the dynamics of biologically relevant systems, which requires the same amount of data as a static structure scaled by the number of time points of interest. Put simply, 10 frames of motion would require 10 times more data than a static structure of equal quality.

The early user experiments at the EuXFEL have been invaluable in demonstrating the capabilities of SFX experiments at MHz rates. MHz SFX lends itself to more data collection in less time and therefore also better statistical analysis of difficult datasets than previously possible at lower-repetition-rate SFX facilities. For this reason, MHz SFX encourages novel experiments. Pump–probe experiments can investigate samples that have short-lived, optically-excited states or transient states while undergoing conformational change. Shortly before the X-ray pulse probes a sample, an additional external light source is transported to the interaction region to “pump” the sample into an excited or transient state. The time between pump and probe can be labelled as Δt . Pump–probe experiments are most easily demonstrated with the use of an optical laser (the “pump”), where that laser interacts with an optically sensitive protein, such as PSI or PSII (Photosystem II, or water–plastoquinone oxidoreductase), before being probed by the X-ray pulse. Light-sensitive proteins are thought to go through many conformational changes before relaxing into a stable state. Observing and determining these conformational changes elucidates never-before-seen interactions, opening the possibility for future applications. Pump–probe experiments have been successful at LCLS [62] and other FELs [63]; however, with the newly available MHz source at EuXFEL, SPB/SFX is now opening up new frontiers into more rapid data collection of transient protein structures.

As early as September 2019, Pandey et al. published successful femtosecond time-resolved SFX data collected at the SPB/SFX instrument at a MHz rate [64]. The photocycle of photoactive yellow protein (PYP) contained previously unknown transient states. PYP is a bacterial photosensor that undergoes a conformational photocycle consisting of many intermediates. The changes between

states occur across a large range of temporal resolutions, from picoseconds to milliseconds. Structural information exists for most of the states within the photocycle, though spectroscopy data suggest a novel confirmation in the range of 1 to 100 picoseconds after entering the excitation state pG^* , Figure 10.

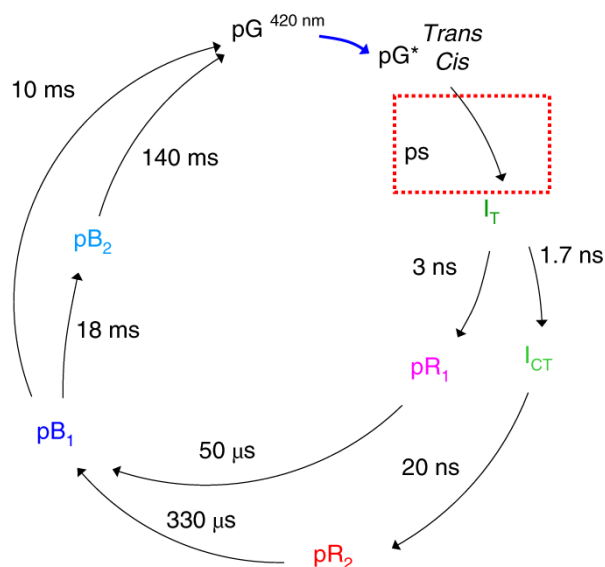


Figure 10. Photocycle of photoactive yellow protein. The red box highlights a region where previously unseen structural confirmations exist, as determined by spectroscopy. Figure originally published in Nat. Methods [64].

PYP has been of significant interest due to its potential use in optically controlled biological reactions. Previously, Pandey et al. were able to determine the 3 ps time point at LCLS and the 100 ps time point at APS during separate experiments. Another experiment, conducted at SPB/SFX, injected PYP at 30 m s^{-1} and matched with a 0.5 MHz intra-train rate, as supported by Wiedorn et al. [50]. The final experimental setup illuminated the sample 10 ps before the arrival of the second pulse. Each X-ray pulse was separated by $1.78 \mu\text{s}$, and each laser pulse was separated by $7.1 \mu\text{s}$. The resulting data collection returned four different time points as measured from the initial illumination (10 ps and 1.78, 3.56, and $5.33 \mu\text{s}$). Shown in Figure 11, the laser illumination overlapped with the second, third, and fourth pulses and kept the first pulse dark, or not illuminated, then repeated this pattern across the entire pulse train. This experimental design simultaneously collected data from potentially three different protein confirmations and a dark control, Figure 12.

Thanks to the three additional time points collected at the SPB/SFX instrument, in conjunction with the two previously measured time points, Pandey et al. were able to show that the torsional angle of the chromophore tail changes from 172° while dark, to 39° at 3 ps, to 51° at 10 ps, and to 54° at 30 ps before relaxing to 30° at 100 ps. Further details by Pandey et al. explain how the fast action of the photon absorption causes the chromophore head to twist over a relatively slow 100 ps before moving into one of two possible intermediate states.

Each possible pulse in a pulse train is separated by an integer multiple of 220 ns. The train can be filled with any configuration of pulses, up to the maximum train length of $600 \mu\text{s}$. In conjunction with the X-ray pulse-pattern design, the laser-induced pump timing can also be flexibly delivered with femtosecond resolution, allowing for excellent control over the design of pump–probe experiments.

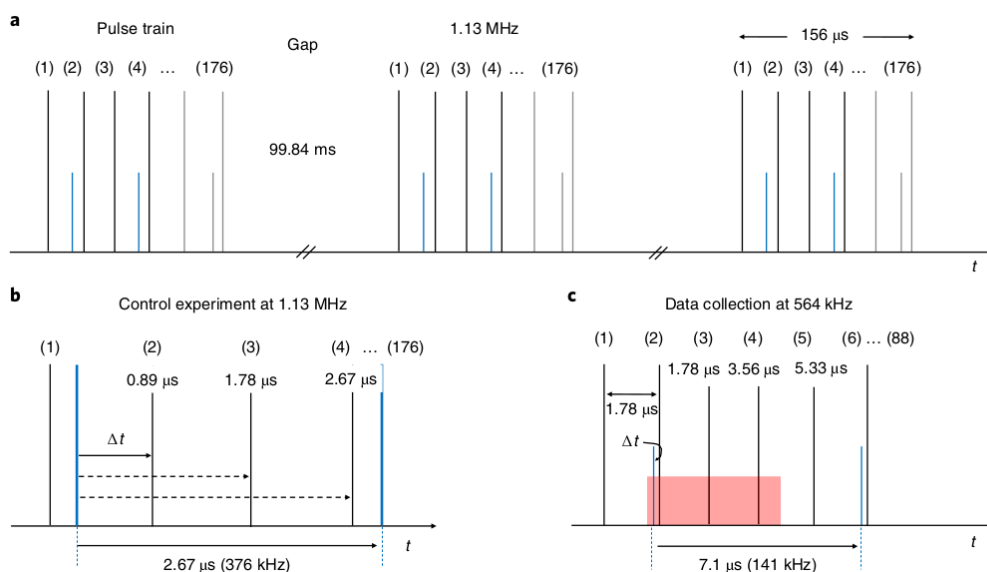


Figure 11. Pump-probe timing schematic. Black lines indicate X-ray pulse timing. (a) A schema showing that there are 176 X-ray pulses in each train at 1.1 MHz, with a 99 ms gap between trains. Blue lines indicate the laser probe timing relative to the X-ray probe arrival. (b) The Δt schema at 1.1 MHz. (c) The 0.5 MHz timing schema. The red box indicates that the length of the pump laser duration overlaps with three X-ray pulses before leaving the 5.33 μ s X-ray pulse unilluminated. Figure originally published in Nat. Methods [64].

Pandey et al. discuss how previous tr-SFX timepoints had to be collected over numerous datasets and over weeks of beamtimes; however, advancements in MHz repetition at the EuXFEL now make it possible to collect enough data within a single experiment. This significant advancement in repetition rate provides the means to thoroughly elucidate multiple time points quickly, resulting in more data and a more detailed understanding of structural dynamics and its relationship to biological function.

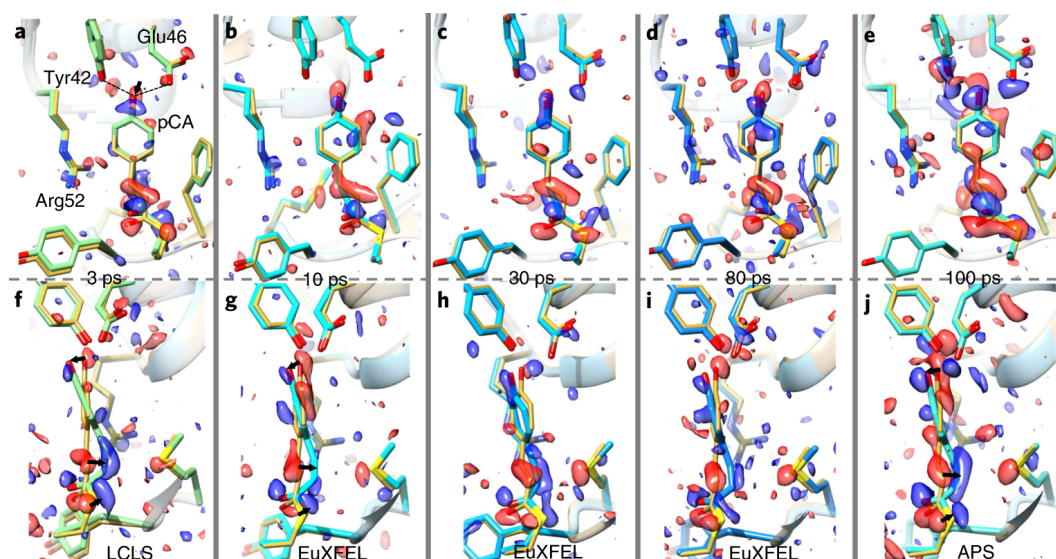


Figure 12. A Time series of the chromophore binding region of photoactive yellow protein (PYP) between 3 and 100 ps. A difference electron density map is shown in red (-3σ contour level) and blue ($+3\sigma$ contour level). Images (a–e) show a “front” view, images (f–j) show a side view. Arrows highlight regions of displacement. Figure originally published in Nat. Methods [64].

2. A More Flexible MHz, Serial Crystallography Experiment

Through optimizing parameters such as resolution, detector geometry, and focal size, the SPB/SFX instrument is leading the charge in next-level MHz SFX experiments and advancing the capabilities to produce movie-like protein dynamics.

It is evident that the unprecedented MHz repetition rate SFX experiments now possible at the EuXFEL provide vast quantities of quality data for better statistical analysis than is currently possible at other XFELs. The experiments mentioned herein demonstrate the novel capabilities of the EuXFEL and provide examples for future research. At the time of writing, preliminary experiments have already utilized a 4.5 MHz pulse rate with 250 pulses per train, and future experiments have access to more than double the rate of data collection than that of Yefanov et al., while also decreasing the minimum time point separation by a factor of 4.

Currently, improvements are under way to increase the number of pulses per train so as to fill all AGIPD memory cells with 352 frames per train, that is, 3520 frames measured per second. Initial plans to implement a veto system are also in discussion, with the goal to increase the number of data-containing frames measured per train. At present, data are collected regardless of whether diffraction is present, resulting in a typical 1% hit rate for GDVN sample injection. Detection of crystal–X-ray interaction prior to detector read-out could effectively use more than 352 pulses per train, where the frames that do not contain data are overwritten in the memory cells. This potentially allows for up to 352 data-containing images recorded per train.

Further improvements in detectors include the development of an AGIPD 4 Mpx detector (AGIPD-4M). Design specifications for AGIPD-4M use the same-sized 200 μm^2 pixels as its smaller 1 Mpx cousin [48]. AGIPD-4M is therefore four times bigger and, as discussed in Section 1.8, a larger detector will provide better flexibility in experimental design in cases similar to those discussed by Gisriel et al. [56].

Mixing Experiments at MHz Pulse Rates

Mixing SFX experiments, for a variety of time points, is made viable by the increased data collection rate and advancements in reliable sample jetting. Past crystallographic experiments could easily determine structural changes between pre- and post-binding states. However, only recently, with the use of XFELs, have researchers been able to measure intermediate conformations during ligand binding using mixing SFX experiments [65]. Mixing experiments involve the introduction of one solution to (typically) a crystal suspension to invoke a reaction just prior to X-ray interaction. At that point, the time of interest can be investigated by increasing the travel distance between mixing and probing, much like for pump–probe experiments. Any reagent mixed with a crystal suspension ideally requires immediate diffusion into the crystal core for a reaction to occur simultaneously, so as to achieve true homogeneity of the protein's conformational state. This is, of course, impossible in practice. A detailed explanation of the diffusion of reagents into crystals goes beyond the scope of this review; however, it is worth mentioning that a decrease in crystal size results in a decrease in the time until homogeneity [66,67]. For example, Schmidt et. al. show that a cube-shaped crystal with dimensions of $400 \times 400 \times 1600 \mu\text{m}^3$ will have a diffusion time of tens of seconds, while crystals more appropriately sized for SFX injection, that is, $0.5 \times 0.5 \times 0.5 \mu\text{m}^3$, will have a diffusion time of 17 μs [67]. Therefore, the coincidental benefit of using nanocrystals over larger crystals is a decrease in the time to reach homogeneity, allowing the recording of faster time points in dynamical systems. Functional mixing jets have already proven effective at other XFEL facilities [68,69], and similar experiments will be possible at the EuXFEL SPB/SFX instrument—just at much higher data rates. Measuring transient intermediate states has the potential to experimentally confirm and support movie-like protein dynamics from simulated models, including reactions such as inhibitor binding and much more [70]. Mixing experiments become more viable with the high repetition rates possible at the EuXFEL. Used in collaboration with simulations, such time-resolved mixing experiments will provide valuable and novel insights into binding dynamics.

3. Conclusions

Early experiments at the EuXFEL SPB/SFX instrument have proven successful in providing, for the first time ever, MHz rate, ultrabright X-ray pulses for structure determination. The number of pulses per second possible at the EuXFEL enables unprecedented volumes of data collection. This significant increase in data volume generates improvements in statistics and provides avenues for time-resolved studies in a much shorter experimental timeframe than previously possible. Pump–probe experiments can potentially resolve multiple time points per experiment, as demonstrated by Pandey et al., or analyze statistical changes on a pulse-by-pulse basis, as demonstrated by Yefanov et al.

The publications produced by these first user experiments exemplify the types of unprecedented experimental results and methodology possible at the SPB/SFX instrument of the EuXFEL.

Author Contributions: Conceptualization, G.M. and R.B.; Writing—original draft, G.M.; Writing—review and editing, R.B. and A.P.M. All authors have read and agreed to the published version of the manuscript.

Funding: In addition to the baseline funding provided by the European XFEL members, we acknowledge funding of instrumentation and staff by the following sources: the Wellcome Trust, the German Federal Ministry for Education and Research (BMBF) via projects 05K13GU7 and 05E13GU1, the Ministry of Education, Science, Research and Sport of the Slovak Republic, The Swedish Research Council (822-2013-2014), the Knut and Alice Wallenberg Foundation, the Röntgen-Ångström Cluster, the Swedish Foundation for Strategic Research, the Australian Research Council Center of Excellence in Advanced Molecular Imaging (CE140100011), the Australian Nuclear Science and Technology Organisation (ANSTO), the Max Planck Society for Medical Research, the NSF-STC ‘BioXFEL’ through award STC-1231306, and the Helmholtz Association Strategic Investment funds.

Acknowledgments: We acknowledge European XFEL in Schenefeld, Germany, for provision of X-ray free-electron laser beamtime at Scientific Instrument SPB/SFX and would like to thank the instrument group and facility staff for their assistance. The authors are indebted to the SFX User Consortium for the provision of instrumentation and personnel that has enabled these experiments. The SFX UC is composed of scientific partners from Germany, Sweden, the UK, Slovakia, Switzerland, Australia, and the USA. The authors would also like to thank and acknowledge Kurt Ament and Susanne Fangohr for their careful reading and feedback on the manuscript.

Conflicts of Interest: The authors declare no conflict of interest.

References

1. Watson, J.D.; Crick, F.H. Molecular structure of nucleic acids. *Nature* **1953**, *171*, 737–738. [[CrossRef](#)]
2. Franklin, R.E.; Gosling, R.G. Evidence for 2-chain helix in crystalline structure of sodium deoxyribonucleate. *Nature* **1953**, *172*, 156–157. [[CrossRef](#)] [[PubMed](#)]
3. Helliwell, J.R.; Mitchell, E.P. Synchrotron radiation macromolecular crystallography: Science and spin-offs. *IUCr* **2015**, *2*, 283–291. [[CrossRef](#)] [[PubMed](#)]
4. Rosenbaum, G.; Holmes, K.C.; Witz, J. Synchrotron radiation as a source for X-ray diffraction. *Nature* **1971**, *230*, 434–437. [[CrossRef](#)]
5. Phillips, J.C.; Wlodawer, A.; Yevitz, M.M.; Hodgson, K.O. Applications of synchrotron radiation to protein crystallography: preliminary results. *Proc. Natl. Acad. Sci. USA* **1976**, *73*, 128–132. [[CrossRef](#)]
6. Hendrickson, W.A. Anomalous diffraction in crystallographic phase evaluation. *Q. Rev. Biophys.* **2014**, *47*, 49–93. [[CrossRef](#)]
7. Hendrickson, W.A. Analysis of protein structure from diffraction measurement at multiple wavelengths. *Trans. Am. Crystallogr. Assoc.* **1985**, *21*, 11–21.
8. Kahn, R.; Fourme, R.; Bosshard, R.; Chiadmi, M.; Risler, J.; Dideberg, O.; Wery, J. Crystal structure study of Opsanus tau parvalbumin by multiwavelength anomalous diffraction. *FEBS Lett.* **1985**, *179*, 133–137. [[CrossRef](#)]
9. Bösecke, P.; Diat, O.; Rasmussen, B. High-brilliance Beamline at the European Synchrotron Radiation Facility. *Rev. Sci. Instrum.* **1995**, *66*, 1636–1638. [[CrossRef](#)]
10. Cork, C.; Padmore, H.; McDermott, G.; Hung, L.W.; Henderson, K.; Robinson, A.; Earnest, T. The macromolecular crystallography facility at the Advanced Light Source. *Synchrotron Radiat. News* **1998**, *11*, 18–25. [[CrossRef](#)]

11. Hirata, K.; Kawano, Y.; Ueno, G.; Hashimoto, K.; Murakami, H.; Hasegawa, K.; Hikima, T.; Kumasaka, T.; Yamamoto, M. Achievement of protein micro-crystallography at SPring-8 beamline BL32XU. *J. Phys. Conf. Ser.* **2013**, *425*, 012002. [[CrossRef](#)]
12. Burkhardt, A.; Pakendorf, T.; Reime, B.; Meyer, J.; Fischer, P.; Stübe, N.; Panneerselvam, S.; Lorbeer, O.; Stachnik, K.; Warmer, M.; et al. Status of the crystallography beamlines at PETRA III. *Eur. Phys. J. Plus* **2016**, *131*, 56. [[CrossRef](#)]
13. Altarelli, M. The European X-ray free-electron laser facility in Hamburg. *Nucl. Instrum. Methods Phys. Res. Sect. B Beam Interact. Mater. Atoms* **2011**, *269*, 2845–2849. [[CrossRef](#)]
14. Blundell, T.L. Structure-based drug design. *Nature* **1996**, *384*, 23.
15. Anderson, A.C. The Process of Structure-Based Drug Design. *Chem. Biol.* **2003**, *10*, 787–797. [[CrossRef](#)]
16. Spence, J.C. X-ray lasers for structure and dynamics in biology. *IUCr* **2018**, *5*, 236. [[CrossRef](#)]
17. Kim, K.J. An analysis of self-amplified spontaneous emission. *Nucl. Instrum. Methods Phys. Res. Sect. A Accel. Spectrom. Detect. Assoc. Equip.* **1986**, *250*, 396–403. [[CrossRef](#)]
18. Chapman, H.N.; Caleman, C.; Timneanu, N. Diffraction before destruction. *Philos. Trans. R. Soc. B Biol. Sci.* **2014**, *369*, 20130313. [[CrossRef](#)]
19. Schoenlein, R.; Chattopadhyay, S.; Chong, H.; Glover, T.; Heimann, P.; Shank, C.; Zholents, A.; Zolotarev, M. Generation of femtosecond pulses of synchrotron radiation. *Science* **2000**, *287*, 2237–2240. [[CrossRef](#)]
20. Owen, R.L.; Juanhuix, J.; Fuchs, M. Current advances in synchrotron radiation instrumentation for MX experiments. *Arch. Biochem. Biophys.* **2016**, *602*, 21–31 [[CrossRef](#)]
21. Chapman, H.N.; Fromme, P.; Barty, A.; White, T.A.; Kirian, R.A.; Aquila, A.; Hunter, M.S.; Schulz, J.; DePonte, D.P.; Weierstall, U.; et al. Femtosecond X-ray protein nanocrystallography. *Nature* **2011**, *470*, 73–77. [[CrossRef](#)] [[PubMed](#)]
22. Boutet, S.; Lomb, L.; Williams, G.J.; Barends, T.R.; Aquila, A.; Doak, R.B.; Weierstall, U.; DePonte, D.P.; Steinbrener, J.; Shoeman, R.L.; et al. High-resolution protein structure determination by serial femtosecond crystallography. *Science* **2012**, *337*, 362–364. [[CrossRef](#)] [[PubMed](#)]
23. White, T.A.; Kirian, R.A.; Martin, A.V.; Aquila, A.; Nass, K.; Barty, A.; Chapman, H.N. CrystFEL: A software suite for snapshot serial crystallography. *J. Appl. Crystallogr.* **2012**, *45*, 335–341. [[CrossRef](#)]
24. Gevorkov, Y.; Barty, A.; Brehm, W.; White, T.; Tolstikova, A.; Wiedorn, M. O.; Meents, A.; Grigat, R.-R.; Chapman, H. N.; Yefanov, O. pinkIndexer—A universal indexer for pink-beam X-ray and electron diffraction snapshots. *Acta Crystallogr. Sect. A Found. Adv.* **2020**, *76*, 121–131. [[CrossRef](#)] [[PubMed](#)]
25. Stellato, F.; Oberthür, D.; Liang, M.; Bean, R.; Gati, C.; Yefanov, O.; Barty, A.; Burkhardt, A.; Fischer, P.; Galli, L.; et al. Room-temperature macromolecular serial crystallography using synchrotron radiation. *Int. Union Crystallogr.* **2014**, *1*, 204–212 [[CrossRef](#)]
26. Gati, C.; Oberthuer, D.; Yefanov, O.; Bunker, R.D.; Stellato, F.; Chiu, E.; Yeh, S.M.; Aquila, A.; Basu, S.; Bean, R.; et al. Atomic structure of granulin determined from native nanocrystalline granulovirus using an X-ray free-electron laser. *Proc. Natl. Acad. Sci. USA* **2017**, *114*, 2247–2252. [[CrossRef](#)]
27. Holton, J.M.; Frankel, K.A. The minimum crystal size needed for a complete diffraction data set. *Acta Crystallogr. Sect. D Biol. Crystallogr.* **2010**, *66*, 393–408. [[CrossRef](#)]
28. Snell, E.H.; Bellamy, H.D.; Borgstahl, G.E. Macromolecular crystal quality. *Methods Enzymol.* **2003**, *368*, 268–288.
29. Boggon, T.; Helliwell, J.; Judge, R.A.; Olczak, A.; Siddons, D.; Snell, E.; Stojanoff, V. Synchrotron X-ray reciprocal-space mapping, topography and diffraction resolution studies of macromolecular crystal quality. *Acta Crystallogr. Sect. D Biol. Crystallogr.* **2000**, *56*, 868–880. [[CrossRef](#)]
30. Chayen, N.E.; Saridakis, E. Protein crystallization: From purified protein to diffraction-quality crystal. *Nat. Methods* **2008**, *5*, 147. [[CrossRef](#)]
31. Chayen, N.; Boggon, T.; Cassetta, A.; Deacon, A.; Gleichmann, T.; Habash, J.; Harrop, S.; Helliwell, J.; Nieh, Y.; Peterson, M.; et al. Trends and challenges in experimental macromolecular crystallography. *Q. Rev. Biophys.* **1996**, *29*, 227–278. [[CrossRef](#)] [[PubMed](#)]
32. McPherson, A.; Gavira, J.A. Introduction to protein crystallization. *Acta Crystallogr. Sect. F Struct. Biol. Commun.* **2014**, *70*, 2–20. [[CrossRef](#)] [[PubMed](#)]
33. Carpenter, E.P.; Beis, K.; Cameron, A.D.; Iwata, S. Overcoming the challenges of membrane protein crystallography. *Curr. Opin. Struct. Biol.* **2008**, *18*, 581–586. [[CrossRef](#)] [[PubMed](#)]
34. Schlichting, I. Serial femtosecond crystallography: The first five years. *IUCr* **2015**, *2*, 246–255. [[CrossRef](#)]

35. Grünbein, M.L.; Shoeman, R.L.; Doak, R.B. Velocimetry of fast microscopic liquid jets by nanosecond dual-pulse laser illumination for megahertz X-ray free-electron lasers. *Opt. Express* **2018**, *26*, 7190–7203. [[CrossRef](#)]
36. Rayleigh, L. On the capillary phenomena of jets. *Proc. R. Soc. Lond.* **1879**, *29*, 71–97.
37. Inguva, V.; Graceffa, R.; Schulz, J.; Bilsel, O.; Perot, B.J. Creating round focused micro-jets from rectangular nozzles. *J. Mech. Sci. Technol.* **2019**, *33*, 4281–4289. [[CrossRef](#)]
38. Weierstall, U. Liquid sample delivery techniques for serial femtosecond crystallography. *Philos. Trans. R. Soc. B Biol. Sci.* **2014**, *369*, 20130337. [[CrossRef](#)]
39. Steinke, I.; Walther, M.; Lehmkuhler, F.; Wochner, P.; Valerio, J.; Mager, R.; Schroer, M.A.; Lee, S.; Roseker, W.; Jain, A.; et al. A liquid jet setup for X-ray scattering experiments on complex liquids at free-electron laser sources. *Rev. Sci. Instrum.* **2016**, *87*, 063905. [[CrossRef](#)]
40. Stan, C.A.; Milathianaki, D.; Laksmono, H.; Sierra, R.G.; McQueen, T.A.; Messerschmidt, M.; Williams, G.J.; Koglin, J.E.; Lane, T.J.; Hayes, M.J.; et al. Liquid explosions induced by X-ray laser pulses. *Nat. Phys.* **2016**, *12*, 966–971. [[CrossRef](#)]
41. Chavas, L.; Gumprecht, L.; Chapman, H. Possibilities for serial femtosecond crystallography sample delivery at future light sources. *Struct. Dyn.* **2015**, *2*, 041709. [[CrossRef](#)] [[PubMed](#)]
42. Altarelli, M.; Brinkmann, R.; Chergui, M.; Decking, W.; Dobson, B.; Düsterer, S.; Grübel, G.; Graeff, W.; Graafsma, H.; Hajdu, J.; et al. The European X-ray Free-Electron Laser Technical Design Report. *DESY* **2006** *97*, 4.
43. Tschentscher, T.; Bressler, C.; Grünert, J.; Madsen, A.; Mancuso, A.; Meyer, M.; Scherz, A.; Sinn, H.; Zastra, U. Photon beam transport and scientific instruments at the European XFEL. *Appl. Sci.* **2017**, *7*, 592. [[CrossRef](#)]
44. Mancuso, A.P.; Aquila, A.; Batchelor, L.; Bean, R.J.; Bielecki, J.; Borchers, G.; Doerner, K.; Giewekemeyer, K.; Graceffa, R.; Kelsey, O.D.; et al. The Single Particles, Clusters and Biomolecules and Serial Femtosecond Crystallography instrument of the European XFEL: Initial installation. *J. Synchrotron Radiat.* **2019**, *26*, 660–676. [[CrossRef](#)] [[PubMed](#)]
45. Dunne, M. *LCLS Strategic Facility Development Plan*; SLAC National Accelerator Laboratory: Menlo Park, CA, USA, 2017; p. 55.
46. Sato, T.; LeTrun, R.; Kirkwood, H.; Liu, J.; Vagovic, P.; Mills, G.; Kim, Y.; Takem, C.; Planas, M.; Emons, M.; et al. Femtosecond timing synchronisation at megahertz repetition rates for an X-ray Free-Electron Laser. *Optica* **2020**. [[CrossRef](#)]
47. Henrich, B.; Becker, J.; Dinapoli, R.; Goettlicher, P.; Graafsma, H.; Hirsemann, H.; Klanner, R.; Krueger, H.; Mazzocco, R.; Mozzanica, A.; et al. The adaptive gain integrating pixel detector AGIPD a detector for the European XFEL. *Nucl. Instrum. Methods Phys. Res. Sect. A Accel. Spectrom. Detect. Assoc. Equip.* **2011**, *633*, S11–S14. [[CrossRef](#)]
48. Allahgholi, A.; Becker, J.; Delfs, A.; Dinapoli, R.; Goettlicher, P.; Greiffenberg, D.; Henrich, B.; Hirsemann, H.; Kuhn, M.; Klanner, R.; et al. The Adaptive Gain Integrating Pixel Detector at the European XFEL. *J. Synchrotron Radiat.* **2019**, *26*, 74–82. [[CrossRef](#)]
49. DePonte, D.; Weierstall, U.; Schmidt, K.; Warner, J.; Starodub, D.; Spence, J.; Doak, R. Gas dynamic virtual nozzle for generation of microscopic droplet streams. *J. Phys. D Appl. Phys.* **2008**, *41*, 195505. [[CrossRef](#)]
50. Wiedorn, M.O.; Oberthür, D.; Bean, R.; Schubert, R.; Werner, N.; Abbey, B.; Aepfelbacher, M.; Adriano, L.; Allahgholi, A.; Al-Qudami, N.; et al. Megahertz serial crystallography. *Nat. Commun.* **2018**, *9*, 4025. [[CrossRef](#)]
51. Grünbein, M.L.; Bielecki, J.; Gorel, A.; Stricker, M.; Bean, R.; Cammarata, M.; Dörner, K.; Fröhlich, L.; Hartmann, E.; Hauf, S.; et al. Megahertz data collection from protein microcrystals at an X-ray free-electron laser. *Nat. Commun.* **2018**, *9*, 3487. [[CrossRef](#)]
52. Yefanov, O.; Oberthür, D.; Bean, R.; Wiedorn, M.O.; Knoska, J.; Pena, G.; Awel, S.; Gumprecht, L.; Domaracky, M.; Sarrou, I.; et al. Evaluation of serial crystallographic structure determination within megahertz pulse trains. *Struct. Dyn.* **2019**, *6*, 064702. [[CrossRef](#)] [[PubMed](#)]
53. Weierstall, U.; James, D.; Wang, C.; White, T.A.; Wang, D.; Liu, W.; Spence, J.C.; Doak, R.B.; Nelson, G.; Fromme, P.; et al. Lipidic cubic phase injector facilitates membrane protein serial femtosecond crystallography. *Nat. Commun.* **2014**, *5*, 1–6. [[CrossRef](#)] [[PubMed](#)]

54. Fromme, R.; Ishchenko, A.; Metz, M.; Chowdhury, S.R.; Basu, S.; Boutet, S.; Fromme, P.; White, T.A.; Barty, A.; Spence, J.C.; et al. Serial femtosecond crystallography of soluble proteins in lipidic cubic phase. *IUCr* **2015**, *2*, 545–551. [[CrossRef](#)]
55. Kupitz, C.; Basu, S.; Grotjohann, I.; Fromme, R.; Zatsepin, N.A.; Rendek, K.N.; Hunter, M.S.; Shoeman, R.L.; White, T.A.; Wang, D.; et al. Serial time-resolved crystallography of photosystem II using a femtosecond X-ray laser. *Nature* **2014**, *513*, 261–265. [[CrossRef](#)]
56. Gisriel, C.; Coe, J.; Letrun, R.; Yefanov, O.M.; Luna-Chavez, C.; Stander, N.E.; Lisova, S.; Mariani, V.; Kuhn, M.; Aplin, S.; et al. Membrane protein megahertz crystallography at the European XFEL. *Nat. Commun.* **2019**, *10*, 1–11. [[CrossRef](#)] [[PubMed](#)]
57. Bénas, P.; Auzeil, N.; Legrand, L.; Brachet, F.; Regazzetti, A.; Riès-Kautt, M. Weak protein–cationic co-ion interactions addressed by X-ray crystallography and mass spectrometry *Acta Crystallogr. Sect. D* **2014**, *70*, 2217–2231 [[CrossRef](#)] [[PubMed](#)]
58. Rossmann, E. Concerning intensity profiles. *Acta Crystallogr. Sect. A Found. Crystallogr.* **2002**, *58*, 12–20. [[CrossRef](#)]
59. Jordan, P.; Fromme, P.; Witt, H.T.; Klukas, O.; Saenger, W.; Krauß, N. Three-dimensional structure of cyanobacterial photosystem I at 2.5 Å resolution. *Nature* **2001**, *411*, 909. [[CrossRef](#)]
60. Szyperski, T. Room Temperature X-Ray Crystallography Reveals Conformational Heterogeneity of Engineered Proteins. *Structure* **2017**, *25*, 691–692. [[CrossRef](#)]
61. Weinert, T.; Olieric, N.; Cheng, R.; Brünle, S.; James, D.; Ozerov, D.; Gashi, D.; Vera, L.; Marsh, M.; Jaeger, K.; et al. Serial millisecond crystallography for routine room-temperature structure determination at synchrotrons. *Nat. Commun.* **2017**, *8*, 542. [[CrossRef](#)]
62. Glowina, J.M.; Cryan, J.; Andreasson, J.; Belkacem, A.; Berrah, N.; Blaga, C.; Bostedt, C.; Bozek, J.; DiMauro, L.; Fang, L.; et al. Time-resolved pump-probe experiments at the LCLS. *Opt. Express* **2010**, *18*, 17620–17630. [[CrossRef](#)] [[PubMed](#)]
63. Kubo, M.; Nango, E.; Tono, K.; Kimura, T.; Owada, S.; Song, C.; Mafuné, F.; Miyajima, K.; Takeda, Y.; Kohno, J.Y.; et al. Nanosecond pump–probe device for time-resolved serial femtosecond crystallography developed at SACLA. *J. Synchrotron Radiat.* **2017**, *24*, 1086–1091. [[CrossRef](#)] [[PubMed](#)]
64. Pandey, S.; Bean, R.; Sato, T.; Poudyal, I.; Bielecki, J.; Villarreal, J.C.; Yefanov, O.; Mariani, V.; White, T.A.; Kupitz, C.; et al. Time-resolved serial femtosecond crystallography at the European XFEL. *Nat. Methods* **2020**, *17*, 73–78. [[CrossRef](#)] [[PubMed](#)]
65. Barends, T.R.; Foucar, L.; Ardevol, A.; Nass, K.; Aquila, A.; Botha, S.; Doak, R.B.; Falahati, K.; Hartmann, E.; Hilpert, M.; et al. Direct observation of ultrafast collective motions in CO myoglobin upon ligand dissociation. *Science* **2015**, *350*, 445–450. [[CrossRef](#)]
66. Geremia, S.; Campagnolo, M.; Demitri, N.; Johnson, L.N. Simulation of Diffusion Time of Small Molecules in Protein Crystals. *Structure* **2006**, *14*, 393–400. [[CrossRef](#)]
67. Schmidt, M. Mix and inject: Reaction initiation by diffusion for time-resolved macromolecular crystallography. *Adv. Condens. Matter Phys.* **2013**, *2013*, 167276. [[CrossRef](#)]
68. Stagno, J.; Liu, Y.; Bhandari, Y.; Conrad, C.; Panja, S.; Swain, M.; Fan, L.; Nelson, G.; Li, C.; Wendel, D.; et al. Structures of riboswitch RNA reaction states by mix-and-inject XFEL serial crystallography. *Nature* **2017**, *541*, 242–246. [[CrossRef](#)]
69. Calvey, G.D.; Katz, A.M.; Schaffer, C.B.; Pollack, L. Mixing injector enables time-resolved crystallography with high hit rate at X-ray free electron lasers. *Struct. Dyn.* **2016**, *3*, 054301. [[CrossRef](#)]
70. Orville, A.M. Entering an era of dynamic structural biology... *BMC Biol.* **2018**, *16*, 55. [[CrossRef](#)]

